

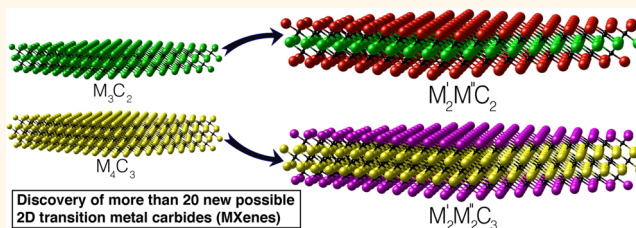


Two-Dimensional, Ordered, Double Transition Metals Carbides (MXenes)

Babak Anasori,^{†,‡,§,#} Yu Xie,^{*,§,#} Majid Beidaghi,^{†,‡,§,#} Jun Lu,^{||} Brian C. Hosler,[†] Lars Hultman,^{||} Paul R. C. Kent,^{§,⊥} Yury Gogotsi,^{*,†,‡} and Michel W. Barsoum^{*,†}

[†]Department of Materials Science & Engineering, Drexel University, Philadelphia, Pennsylvania 19104, United States, [‡]A.J. Drexel Nanomaterials Institute, Drexel University, Philadelphia, Pennsylvania 19104, United States, [§]Center for Nanophase Materials Sciences, Oak Ridge National Laboratory, Oak Ridge, Tennessee 37381, United States, ^{||}Thin Film Physics Division, Department of Physics, Chemistry and Biology (IFM), Linköping University, SE-581 83 Linköping, Sweden, and [⊥]Computer Science and Mathematics Division, Oak Ridge National Laboratory, Oak Ridge, Tennessee 37381, United States. [#]Contributed equally to this work.

ABSTRACT The higher the chemical diversity and structural complexity of two-dimensional (2D) materials, the higher the likelihood they possess unique and useful properties. Herein, density functional theory (DFT) is used to predict the existence of two new families of 2D ordered carbides (MXenes), $M'_2M''C_2$ and $M'_2M''_2C_3$, where M' and M'' are two different early transition metals. In these solids, M' layers sandwich M'' carbide layers. By synthesizing $Mo_2TiC_2T_x$, $Mo_2Ti_2C_3T_x$, and $Cr_2TiC_2T_x$ (where T is a surface termination), we validated the DFT predictions. Since the Mo and Cr atoms are on the outside, they control the 2D flakes' chemical and electrochemical properties. The latter was proven by showing quite different electrochemical behavior of $Mo_2TiC_2T_x$ and $Ti_3C_2T_x$. This work further expands the family of 2D materials, offering additional choices of structures, chemistries, and ultimately useful properties.



KEYWORDS: MXene · 2D materials · DFT calculations · electrochemical properties

Two-dimensional (2D) materials offer high specific surface areas, as well as electronic structures and properties that differ from their bulk counterparts. They also provide easy-to-assemble building blocks for nanoscale architectures.^{1,2} Graphene is the most studied 2D material,^{3–5} but other 2D solids, such as metal oxides and hydroxides, dichalcogenides, hexagonal boron nitride, silicene, and others are garnering increasing attention.^{1,2,6–10} 2D transition metal oxides (TMO) are promising for many applications varying from electronics¹¹ to electrochemical energy storage.^{12,13} By moving toward increasing complexity and diversity, unique combinations of properties can be achieved.

About 4 years ago, we discovered a new class of 2D transition metal carbides and nitrides (Figure 1a) we labeled MXenes,^{14–16} because they are obtained by selectively etching the A-layers from their 3D layered, parent compounds the $M_{n+1}AX_n$, or MAX, phases, where M is an early transition metal, A is an A-group element, such as Al or Si, X is carbon and/or nitrogen, and n is 1–3.¹⁷ The MXenes synthesized to date include

$Ti_3C_2T_x$, Ti_2CT_x , V_2CT_x , Nb_2CT_x , $Nb_4C_3T_x$, and $Ta_4C_3T_x$.¹⁶ In this notation, T_x represents surface groups, mostly O, OH, and F. Solid solutions, such as Ti_3CNT_x , $(Ti_{0.5}Nb_{0.5})_2CT_x$, and $(V_{0.5}Cr_{0.5})_3C_2T_x$ have been reported, in which the two transition elements are believed to randomly occupy the M-sites.¹⁶ MXenes with other M elements such as Sc, Zr, Hf and Mo have been predicted.^{18–20}

MXenes offer a unique combination of metallic conductivity and hydrophilicity, and have already showed promise as electrodes for supercapacitors,²¹ Li–S batteries,²² and Li-, Na- and K-ion batteries,^{14,17,23,24} partially due to a low metal diffusion barrier on their surfaces.^{25,26} MXenes are also predicted to have high capacities for multivalent ions such as Ca^{2+} ,^{24,27} Mg^{2+} and Al^{3+} ,²⁴ and are being explored in many other applications.

In 2014, Liu *et al.* discovered an ordered M_3AX_2 structure, Cr_2TiAlC_2 ,²⁸ in which a Ti-layer is sandwiched between two outer Cr carbide layers in a M_3AX_2 structure. Very recently, we synthesized the first MAX phase with Mo–Al bonds, *viz.* Mo_2TiAlC_2 ,²⁹ wherein Mo-layers sandwiched TiC_2 layers. In short, a new class of ordered MAX phases

* Address correspondence to
gogotsi@drexel.edu,
barsoumw@drexel.edu,
yxе@ornl.gov.

Received for review June 12, 2015
and accepted July 24, 2015.

Published online July 24, 2015
10.1021/acsnano.5b03591

© 2015 American Chemical Society

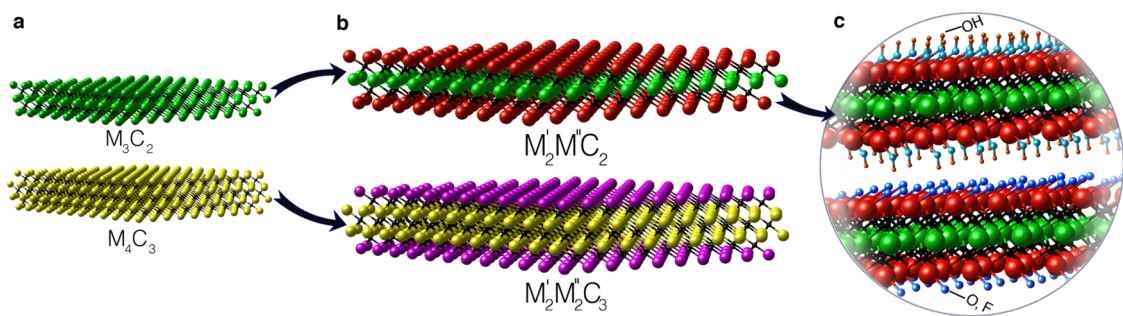


Figure 1. Schematics of the new MXene structures. (a) Currently available MXenes, where M can be Ti, V, Nb, Ta, forming either monatomic M layers or intermixing between two different M elements to make solid solutions. (b) Discovering the new families of double transition metals MXenes, with two structures as $M'_2M''C_2$ and $M'_2M''_2C_3$, adds more than 20 new MXene carbides, in which the surface M' atoms can be different from the inner M'' atoms. M' and M'' atoms can be Ti, V, Nb, Ta, Cr, Mo. (c) Each MXene can have at least three different surface termination groups (OH, O, and F), adding to the variety of the newly discovered MXenes.

is emerging. Their discovery is crucial for the potential expansion of MXene family since they can result in numerous ordered layered 2D structures and MXene chemistries that were not possible previously. However, this discovery does not automatically imply that the corresponding MXenes are realizable because it is not known if the carbide layers are stable in the 2D state when released from the parent MAX phase. Even if the ordered compounds are structurally and energetically stable, they need to survive the etching process. The goal of this article is to demonstrate the existence of ordered double-transition metal 2D carbides.

Herein, we use density functional theory (DFT) to predict the stability of over 20 new, *ordered, double-M* MXenes, viz. $M'_2M''C_2$ and $M'_2M''_2C_3$ (Figure 1b), where M' (outer layer metal) and M'' (inner layer metal) are Ti, V, Nb, Ta, Cr or Mo. In all cases, the C atoms occupy the octahedral sites between the M'–M'' layers. Each M'M''Xene can, in turn, have multiple surface termination groups, T—such as F, O, or OH—greatly expanding their varieties (Figure 1c). Of these, we synthesized Mo_2TiC_2 , $Mo_2Ti_2C_3$ and Cr_2TiC_2 , and showed them to be ordered directly in high-resolution scanning transmission electron microscope (HR STEM) images. We also explored the potential of Mo_2TiC_2 , in electrochemical energy storage and showed that its electrochemical behavior is quite different from $Ti_3C_2T_x$.

RESULTS AND DISCUSSION

Theoretical Prediction of Double Transition Metal MXenes.

We begin by presenting the results of our DFT calculations (see Materials and Methods section for details). Using Mo–Ti containing phases as a case study, we start with Mo_2TiC_2 . The energy differences between a fully ordered Mo_2TiC_2 configuration (inset on far left in Figure 2a) and partially ordered configurations (middle and right insets in Figure 2a and Supporting Information, Figure S1) are plotted in Figure 2a. These results unequivocally show that the ordered Mo_2TiC_2 , with a Mo–Ti–Mo stacking, has the lowest energy. Moreover, the total energy of Mo_2TiC_2 increases almost linearly

as the fraction of Mo atoms in the middle layer increases.

The same calculations were repeated for several other M' and M'' elements in various $M'_2M''C_2$ compositions and select results are shown in Figure 2b. Supporting Information, Figure S2 plots the entire set. On the basis of these figures, it is clear that the stability depends on the elements chosen. Thus, at 0 K, the following MXenes prefer to be in a fully ordered state: Mo_2TiC_2 , Mo_2VC_2 , Mo_2TaC_2 , Mo_2NbC_2 , Cr_2TiC_2 , Cr_2VC_2 , Cr_2TaC_2 , Cr_2NbC_2 , Ti_2NbC_2 , Ti_2TaC_2 , V_2TaC_2 and V_2TiC_2 . The following four MXenes, Nb_2VC_2 , Ta_2TiC_2 , Ta_2VC_2 and Nb_2TiC_2 , are more stable in their partially ordered, than in their fully ordered, state (Figure 2b).

For the $M'_2M''_2C_3$ compositions, there are two fully ordered structures, $M'_2M''_2C_3$ and $M''_2M'_2C_3$ (see Supporting Information, Figure S3). The energy differences between select pairs of fully ordered structures are plotted in Figure 2c, in such a way that the more stable MXene is at 100% (for the full set, see Supporting Information, Figure S2b). Here again, the energy of the system increases monotonically from one ordered configuration to the other. On the basis of these results, we predict that, at 0 K in the absence of terminations, $Mo_2Ti_2C_3$, $Mo_2V_2C_3$, $Mo_2Nb_2C_3$, $Mo_2Ta_2C_3$, $Cr_2Ti_2C_3$, $Cr_2V_2C_3$, $Cr_2Nb_2C_3$, $Cr_2Ta_2C_3$, $Nb_2Ta_2C_3$, $Ti_2Nb_2C_3$, $Ti_2Ta_2C_3$, $V_2Ta_2C_3$, $V_2Nb_2C_3$ and $V_2Ti_2C_3$ are ordered. Since, by our definition the first element in the formula is on the surface, their opposite configurations (e.g., $Ti_2Mo_2C_3$, $V_2Cr_2C_3$, etc.) are higher in energy. From the totality of these results one can infer two important generalizations concerning ordering. The Mo and Cr atoms avoid the middle layers, whereas the Ta and Nb, when given the chance, avoid the outer ones. It is important to know that the inclusion of entropy³⁰ and/or surface terminations in these calculations could affect the degree of order.

To further explore the driving forces for ordering, we calculated the formation energies of various single M M_3C_2 and M_4C_3 structures, from their elements (Table 1). These results indicate that Mo_3C_2 and

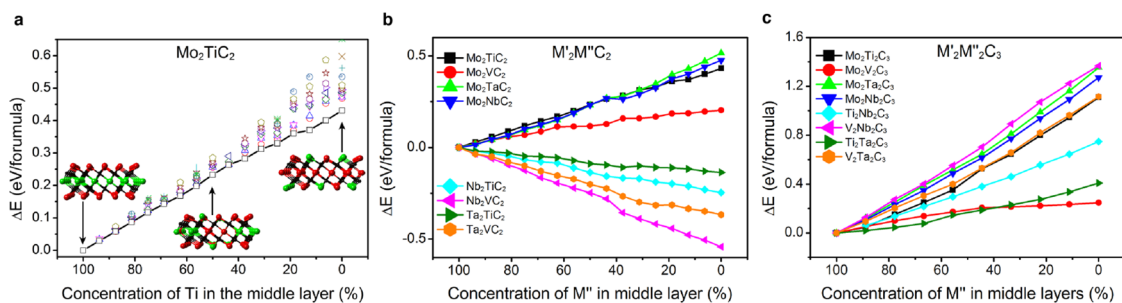


Figure 2. Predicted stability of $\text{M}'\text{M}''\text{Xenes}$ based on DFT calculations. (a) Total energy diagram of Mo_2TiC_2 monolayer as a function of Ti concentration in the middle layer, relative to fully ordered Mo_2TiC_2 . The open symbols are the calculated total energies for both ordered and disordered Mo_2TiC_2 configurations. For all concentrations, the lowest energy configurations (squares) correspond to the most ordered configuration calculated. The black line is a guide for the eye for the lowest energy configuration of each composition. Insets show the stable structures of Mo_2TiC_2 monolayers with 100%, 50%, and 0% Ti in the middle layer (Ti atoms are green, Mo atoms are red, and C atoms are black). The stable structure of $\text{Mo}_2\text{Ti}_2\text{C}_3$ monolayers is shown in Figure 4d. (b and c) Total energy diagrams of calculated $\text{M}'_2\text{M}''\text{C}_2$ (b) and $\text{M}'_2\text{M}''_2\text{C}_3$ (c) MXenes.

TABLE 1. Formation Energies (eV/atom) from Their Elements of Select M_3C_2 and M_4C_3 Unterminated MXenes

unterminated MXenes	formation energy (eV/atom)					
	transition metal (M)					
	Ti	V	Nb	Ta	Cr	Mo
M_3C_2	-0.365	-0.254	0.039	-0.017	0.012	0.328
M_4C_3	-0.594	-0.582	-0.236	-0.259	-0.092	0.258

Mo_4C_3 are highly unstable and are thus unlikely to be synthesized. These results do not mean that Mo–C bonds are unstable but rather that the Mo and C atoms avoid, at all costs, to stack in a face centered cubic (fcc) arrangement characteristic of the M_{n+1}X_n layers. DFT calculations have shown that hexagonal molybdenum carbides are more stable than their rock salt counterparts.³¹ Consequently, if Mo_3C_2 and Mo_4C_3 are formed, Mo and C would be in fcc arrangement, which makes them energetically less preferable. By adding an element that favors the fcc arrangement with C, *viz.* Ti, the Mo layers avoid the fcc arrangement with the C atoms, forming Mo_2TiC_2 or $\text{Mo}_2\text{Ti}_2\text{C}_3$ instead. Consistent with this notion is that most binary Mo-carbide phases are hexagonal.³¹ The same notion explains why the Cr atoms (Table 1) also prefer the outside of the M_{n+1}C_n layers.

To shed light on effects of chemistry on the electronic properties of $\text{Mo}_2\text{TiC}_2\text{T}_x$ and its end members as a function of T where T = OH, O and F, we carried out further DFT calculations and plotted the projected and total density of states (DOS) (Figure 3). In all cases and regardless of termination, the DOS at Fermi level (E_f) is dominated by the M–M d-orbitals and is substantial. In the $\text{Mo}_2\text{TiC}_2\text{T}_x$ case (Figure 3a–c), the DOS at E_f is dominated by the Mo–Mo d-orbitals and *not* the Ti orbitals. Thus, the Mo layers should control its electronic properties.

Synthesis of Double Transition Metal MXenes. On the basis of these predictions, we chose to synthesize Mo_2TiC_2 , $\text{Mo}_2\text{Ti}_2\text{C}_3$ and Cr_2TiC_2 not only because they would

serve as typical examples of ordered $\text{M}'_2\text{M}''\text{C}_2$ and $\text{M}'_2\text{M}''_2\text{C}_3$, but also because neither Mo- nor Cr-based single-transition metal MXenes exist to date. Synthesis of the MXenes followed published protocols (see Materials and Methods).

In agreement with the disappearance of the MAX phase peaks in the X-ray diffraction (XRD) patterns after etching (Figure 4a,b), energy dispersive X-ray spectroscopy (EDX) confirmed a significant drop in the Al signals and concomitant increases in the F and O signals (see Supporting Information, Table S2), implying that our MXene surfaces are O, OH and F terminated.^{16,32} The MXene yield was close to 100%.

A comparison of the XRD patterns of $\text{Mo}_2\text{TiAlC}_2$ before—lower red pattern, Figure 4a—and after etching and delamination (middle green and top blue patterns, respectively, in Figure 4a) clearly shows that all peaks belonging to $\text{Mo}_2\text{TiAlC}_2$ were replaced by $(000l)$ peaks belonging to $\text{Mo}_2\text{TiC}_2\text{T}_x$. These peaks broaden and downshift to lower angles, which is due to an increase in the *c* lattice parameter, LPs, from 18.6 Å in $\text{Mo}_2\text{TiAlC}_2$ to 25.8 and 30.5 Å after etching and delamination, respectively (Figure 4a). Consistent with our previous results on V_2CT_x , Nb_2CT_x ,¹⁷ and $\text{Nb}_4\text{C}_3\text{T}_x$,³³ the large *c*-LPs, increases upon etching are due to the presence of intercalated water and, quite possibly, cations between the MXene sheets. The widening of the $(000l)$ peaks is related to domain size reduction along [0001] due to the etching process. That the *c*-LP increases further after delamination (compare middle and top patterns in Figure 4a) most probably reflects the presence of additional water layers between the MXene sheets, like in $\text{Nb}_4\text{C}_3\text{T}_x$.³³

It is important to note here that the $(11\bar{2}0)$ peak, around 62° , is present after etching (compare green and red in Figure 4a), but disappears after delamination (top blue pattern in Figure 4a). On the basis of our previous work, this indicates that etching alone does not necessarily disrupt the stacking along nonbasal directions.²¹ The disappearance of this peak upon delamination proves that when the delaminated layers

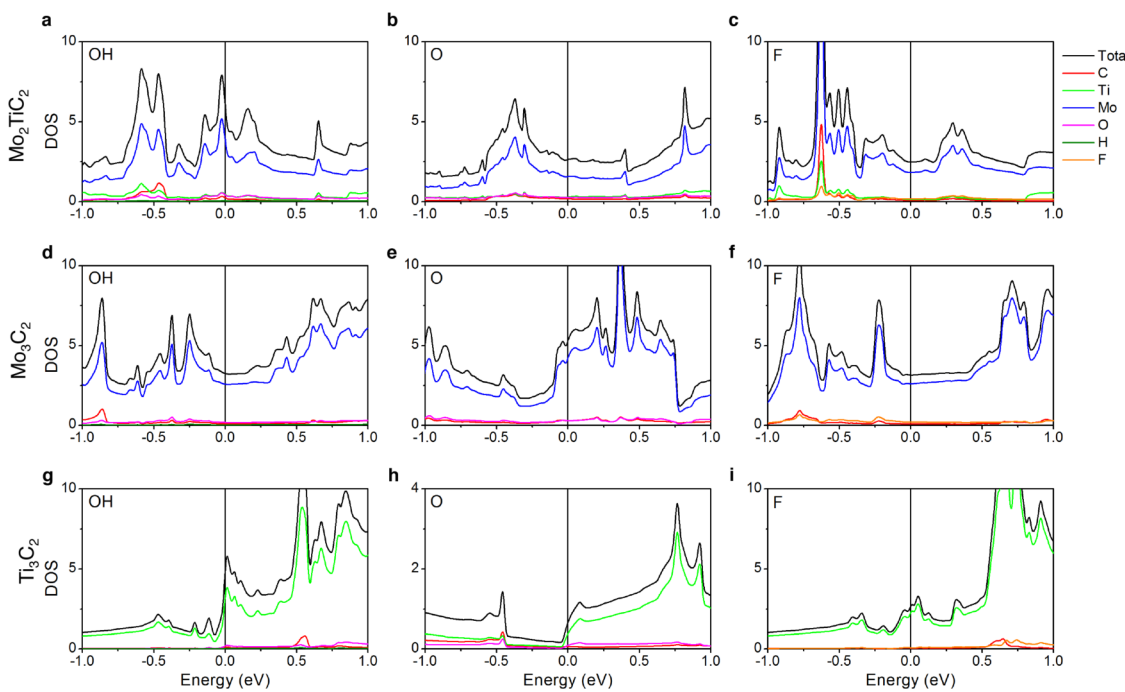


Figure 3. Electronic structures of selected MXenes. (a–i) Total and projected densities of states for OH-, O-, and F-terminated Mo_2TiC_2 (a–c), Mo_3C_2 (d–f), and Ti_3C_2 (g–i) MXenes.

are restacked they do so randomly, while still maintaining crystallographic ordering along [0001]. The exact same conclusions can be reached for $\text{Mo}_2\text{Ti}_2\text{C}_3$ (Figure 4b). In this case, the c-LP of the starting $\text{Mo}_2\text{Ti}_2\text{AlC}_3$ powder is about 23.6 Å (bottom pattern in Figure 4b) and increases to 34.6 Å after delamination (top pattern in Figure 4b), with that of the etched sample (middle pattern in Figure 4b) in between.

Scanning electron microscope (SEM) images of the parent MAX phases (Figure 4e,j), and their MXenes (Figure 4f,k) confirm the 3D to 2D transformation in both materials, as schematically shown in Figure 4c,d. So do HR STEM images of $\text{Mo}_2\text{TiAlC}_2$ and $\text{Mo}_2\text{TiC}_2\text{T}_x$ shown in Figure 4, panels g and h, respectively. In the former, the Mo–Ti layers are interleaved with Al layers; in the latter, the Al is absent. The atomic ordering of the Mo and Ti layers was confirmed by EDX mapping (Supporting Information, Figure S4), in which a layer of Ti (green) is sandwiched between two Mo layers (red). Lower magnification TEM image of $\text{Mo}_2\text{TiC}_2\text{T}_x$ flakes (Figure 4i) clearly shows its layered nature, even after etching. It is this order that gives rise to peaks $\approx 62^\circ$ in the XRD patterns. A TEM image of a Mo_2TiC_2 flake and a low-magnification image of Mo_2TiC_2 layers are shown in Supporting Information Figures S5 and S6a, respectively.

A comparison of the HR STEM images of $\text{Mo}_2\text{Ti}_2\text{AlC}_3$ (Figure 4l) and $\text{Mo}_2\text{Ti}_2\text{C}_3\text{T}_x$ (Figure 4m,n) again clearly evidence the removal of the Al layers by etching. The ordering of the Mo and Ti atoms, confirmed by EDX mapping (Supporting Information, Figure S4), is highlighted by red and green circles, respectively, in

Figure 4l,m. After etching, the gaps between the MXene layers along [0001] are no longer as evenly spaced as they were in the parent phase (compare Figure 4g,h, or Figure 4l,n). A low-magnification TEM image of the $\text{Mo}_2\text{TiC}_2\text{T}_x$ layers is shown in Supporting Information, Figure S6b.

When $\text{Cr}_2\text{TiAlC}_2$ powders were etched in 6 M HCl with 5 mol equiv of LiF, for 42 h at 55 °C, a characteristic MXene peak emerged (Supporting Information, Figure S7), presumably that of $\text{Cr}_2\text{TiC}_2\text{T}_x$. The c-LP was 24.3 Å. However, in contrast to $\text{Mo}_2\text{TiC}_2\text{T}_x$ (Figure 4a), we were not able to achieve 100% yield (see Supporting Information, Table S2), and completely rid the etched powders of the parent MAX phase. The same was true of $\text{Mo}_2\text{Ti}_2\text{AlC}_3$ (Figure 4b). Consequently, we focused the electrochemical work described below on the purest of the three, *viz.* $\text{Mo}_2\text{TiC}_2\text{T}_x$.

Previous studies have shown that MXenes multilayers could be delaminated to single, or few-layer, MXene flakes by intercalation and sonication.²³ Here, $\text{Mo}_2\text{TiC}_2\text{T}_x$ was delaminated by first intercalating dimethyl sulfoxide (DMSO) between the layers, followed by sonication in water,²³ as shown schematically in Figure 5a. After delamination, a stable $\text{Mo}_2\text{TiC}_2\text{T}_x$ colloidal solution was obtained (Figure 5b), which, in turn, was used to form freestanding conductive $\text{Mo}_2\text{TiC}_2\text{T}_x$ 'paper'²³ (Figure 5c,d) by vacuum-assisted filtration.

Electrochemistry of $\text{Mo}_2\text{TiC}_2\text{T}_x$. Since $\text{Ti}_3\text{C}_2\text{T}_x$, Ti_2CT_x and other MXenes have previously shown promising performance in energy storage devices,^{17,23,34} we tested $\text{Mo}_2\text{TiC}_2\text{T}_x$ 'paper' as electrodes for Li-ion batteries (LIBs). To prove that the Mo-layers are at the surface

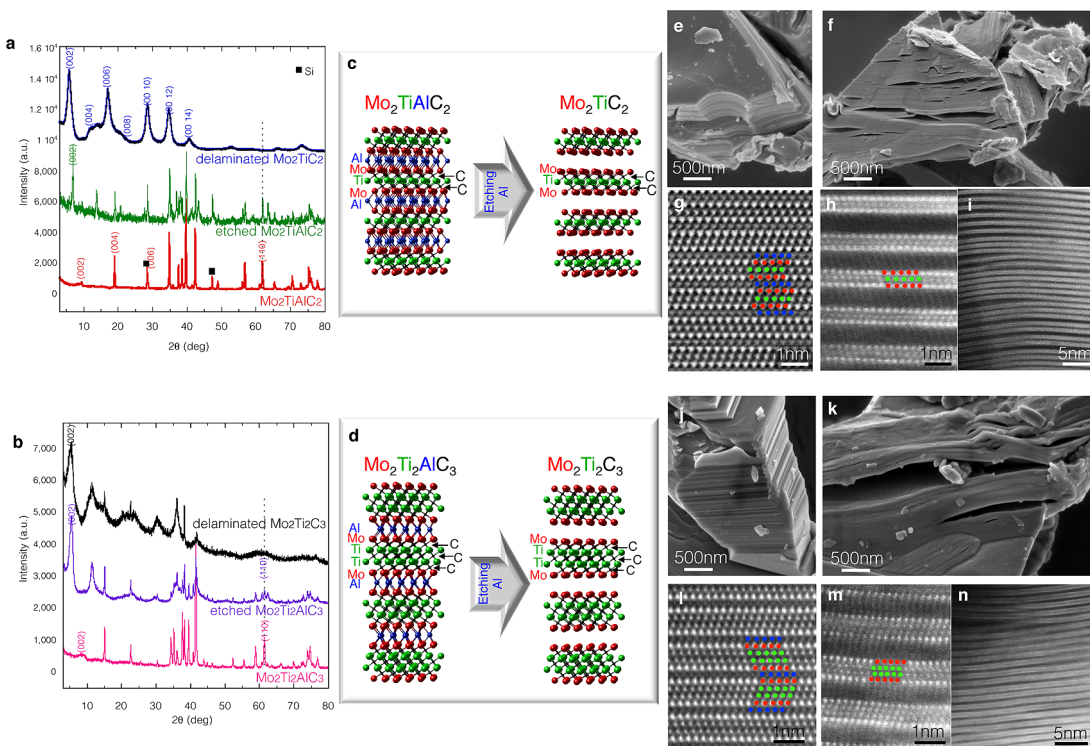


Figure 4. Synthesis and structure of Mo_2TiC_2 and $\text{Mo}_2\text{Ti}_2\text{C}_3$. (a) XRD patterns of $\text{Mo}_2\text{TiAlC}_2$ before (red) and after (green) HF treatment and after delamination (blue). In the delaminated sample, only *c*-direction peaks, $(00l)$ peaks, are visible, corresponding to a *c* lattice parameter of 30.44 \AA ; the (110) peak is no longer observed, showing loss of order in nonbasal directions. (b) XRD patterns of $\text{Mo}_2\text{Ti}_2\text{AlC}_3$ before (pink) and after (purple) HF treatment and after delamination (black). (c and d) Schematics of $\text{Mo}_2\text{TiAlC}_2$ to $\text{Mo}_2\text{TiC}_{2\text{Tx}}$ and $\text{Mo}_2\text{Ti}_2\text{AlC}_3$ to $\text{Mo}_2\text{Ti}_2\text{C}_{3\text{Tx}}$ transformations; red, green, blue, and black circles represent Mo, Ti, Al, and C atoms, respectively. (e and f) SEM images of $\text{Mo}_2\text{TiAlC}_2$ and $\text{Mo}_2\text{TiC}_{2\text{Tx}}$, respectively. Note the layers become open after etching in $\text{Mo}_2\text{TiC}_{2\text{Tx}}$. (g and h) HRSTEM of $\text{Mo}_2\text{TiAlC}_2$ and $\text{Mo}_2\text{TiC}_{2\text{Tx}}$, respectively. Atoms are shown with the same colors as (c). Atomic ordering is confirmed by EDX mapping. No Al was observed in EDX of $\text{Mo}_2\text{TiC}_{2\text{Tx}}$. (i) Lower magnification TEM image of (f) showing the layered structure throughout the sample. (j and k) SEM images of $\text{Mo}_2\text{Ti}_2\text{AlC}_3$ and $\text{Mo}_2\text{Ti}_2\text{C}_{3\text{Tx}}$, respectively. HRSTEM images of (l) $\text{Mo}_2\text{Ti}_2\text{AlC}_3$ and (m and n) $\text{Mo}_2\text{Ti}_2\text{C}_3$. Atoms are shown with the same colors as (d).

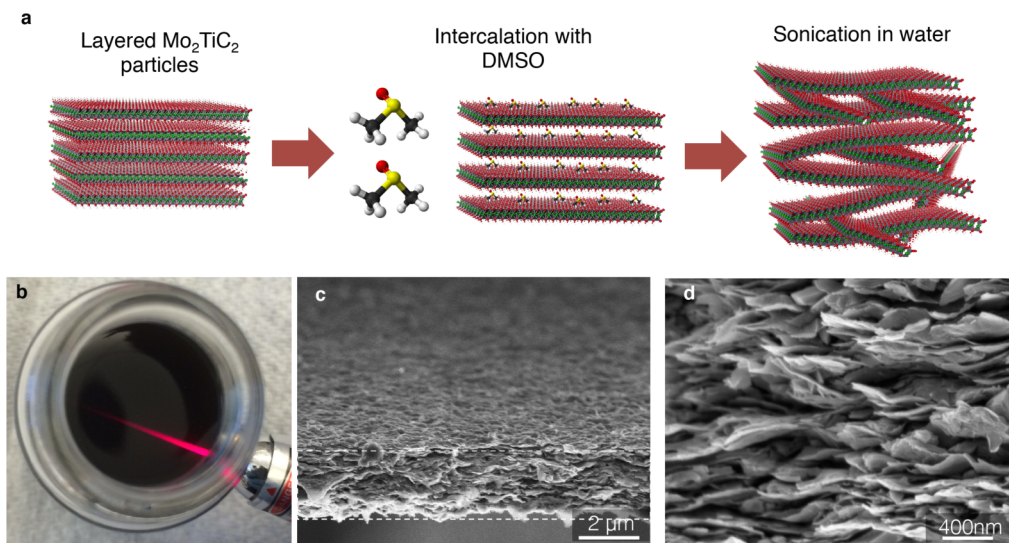


Figure 5. Delamination of Mo_2TiC_2 . (a) Schematic showing delamination process used to produce single or few-layered Mo_2TiC_2 sheets. (b) Photograph shows the Tyndall effect on a stable colloidal solution of Mo_2TiC_2 in water. Low (c) and high (d) magnification cross-sectional SEM image of freestanding Mo_2TiC_2 'paper' fabricated by filtration of a stable colloidal solution; dotted lines in (c) show the film's cross section. MXene flakes are well aligned, but not too tightly packed in the 'paper'.

and dictate the surface properties, we compared the electrochemical properties of $\text{Mo}_2\text{TiC}_{2\text{Tx}}$ to those of

$\text{Ti}_3\text{C}_2\text{T}_x$. The cyclic voltammetry (CV) curves (Supporting Information, Figure 8a) show that much of the lithiation

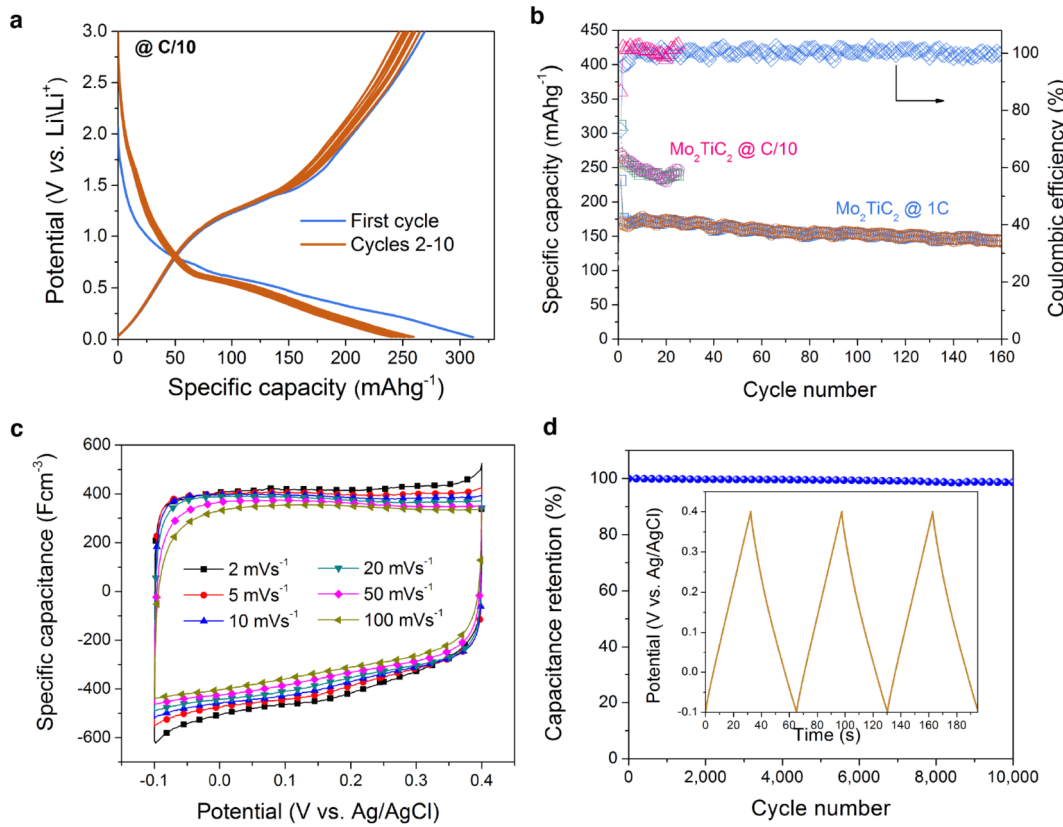


Figure 6. Electrochemical performance of Mo₂TiC₂ in LIB and supercapacitor electrodes. (a) Voltage profiles between 0.02 and 3 V vs Li/Li⁺ at C/10 rate for the first 10 cycles. (b) Specific lithiation (squares) and delithiation (circles) capacities versus cycle number at 1 C and C/10 rates. Right axis in panel (b) shows the Coulombic efficacies for cells tested at these rates. (c) Cyclic voltammograms, at different scan rates, for a freestanding electrode in 1 M H₂SO₄. (d) Capacitance retention test of Mo₂TiC₂ 'paper' in 1 M H₂SO₄. Inset shows galvanostatic cycling data collected at a current density of 1 A/g.

happens at voltages less than ~0.6 V vs Li/Li⁺. However, and although there is a broad peak at ~1.3 V during charging, delithiation continues up to a voltage of 3 V. A crucial and important distinction between previous and current results is the fact that here 85% of the total capacity is below 1 V compared to <66% for Nb₂CT_x.¹⁷

The discharge profile for a sample tested at a rate of C/10 (Figure 6a) shows a voltage plateau starting at about 0.6 V, consistent with the appearance a discharge peak in the CVs (Supporting Information, Figure S8a). The first cycle discharge and charge capacities, at C/10, are about 311 and 269 mA·h g⁻¹, respectively, which translates to a Coulombic efficiency of 86%. The reason for this initial irreversible capacity is to be studied. After a few cycles, however, the Coulombic efficiency approaches 100% (Figure 6b). The first cycle irreversible capacities reported here (14% at C/10 and 27% at 1 C) are significantly lower than the 45–60% reported for other MXenes.^{14,17,23} At 1 C, the Mo₂TiC₂T_x electrode showed a stable capacity of about 176 mA·h g⁻¹ at the second cycle and retains about 82% of this capacity after 160 cycles (Figure 6b). About 92% of the capacity of 260 mA·h g⁻¹ is retained after 25 cycles at C/10. At both rates, Coulombic efficiencies higher than 97% were observed after the first cycle.

TABLE 2. Calculated Li Adsorption Energies (eV/atom) of OH- and O-Terminated Mo₂TiC₂, Mo₃C₂, and Ti₃C₂^a

surface termination	Li adsorption energy (eV/atom)		
	MXene composition	Mo ₂ TiC ₂	Mo ₃ C ₂
OH		0.07	0.03
O		-1.63	-1.68

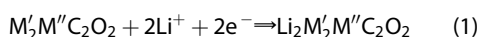
^a Note similarity between the two Mo-containing MXenes.

The fact that Mo₂TiC₂T_x and Ti₃C₂T_x are isostructural and only differ in the nature of their surface atoms, and yet exhibit significantly difference electrochemical behavior, is indirect evidence that the Ti atoms do not play a major role in the electrochemical behavior of Mo₂TiC₂T_x and the latter acts as a pure Mo MXene.

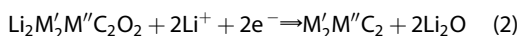
To understand why Mo₂TiC₂T_x and Ti₃C₂T_x behave differently, we compared Li adsorption on OH- and O-terminated Mo₂TiC₂T_x, Ti₃C₂T_x and Mo₃C₂T_x (Table 2) and show that Li would rather adsorb onto the O terminations than the OH-ones. The fact that the adsorption energies for Mo₂TiC₂T_x and Mo₃C₂T_x surfaces are comparable and lower than those for Ti₃C₂T_x

confirms that the Mo-outer layers dominate the surface properties. Given that $\text{Mo}_3\text{C}_2\text{T}_x$ is unstable (Table 1), the utility of having the ordered phases becomes clear.

The estimated theoretical Li capacity is 43 and $181 \text{ mA}\cdot\text{h g}^{-1}$ for OH- and O-terminated Mo_2TiC_2 , respectively. Since the capacity of the OH-terminated Mo_2TiC_2 is much smaller than the measured one $\sim 150 \text{ mA}\cdot\text{h g}^{-1}$, the lithiation should occur on the O terminations. Previous studies^{26,35} have shown that OH termination on MXene surfaces can be converted to O termination with metal ion adsorption. Therefore, the following lithiation reaction can be envisioned after the first cycle:



Although the predicted Li capacity of $\text{Mo}_2\text{TiC}_2\text{O}_2$ is close to experiments $\sim 150 \text{ mA}\cdot\text{h g}^{-1}$, the lithium insertion into interlayer spacing of MXene sheets should occur at $\sim 1.6 \text{ V vs Li/Li}^+$, which is much higher than the voltage where much of the lithiation happens ($\sim 0.6 \text{ V vs Li/Li}^+$). Further simulations suggest that a conversion reaction:



may also be possible. The enthalpy changes for eq 2 are -0.74 , -0.87 , and $+0.54 \text{ eV/formula unit}$ for $\text{Mo}_2\text{TiC}_2\text{O}_2$, $\text{Mo}_3\text{C}_2\text{O}_2$, and $\text{Ti}_3\text{C}_2\text{O}_2$, respectively. Clearly, the reaction is energetically favorable for Mo-based MXenes, but not for $\text{Ti}_3\text{C}_2\text{O}_2$. Thus, below 0.7 V vs Li/Li^+ , reaction eq 2 should occur in $\text{Mo}_2\text{TiC}_2\text{O}_2$. The behavior of Mo-based MXenes resembles that of other Mo-based materials.^{36–38} The lithiation in Mo-based MXenes can be described by a two-step mechanism: stage I happens up to a potential of 1.6 V and stage II corresponds to potentials below 0.6 V . This mechanism may well explain why: (i) a voltage plateau is obtained in the Mo-case, and (ii) the voltage profiles of $\text{Ti}_3\text{C}_2\text{T}_x$ are different from $\text{Mo}_2\text{TiC}_2\text{T}_x$. With the extra Li ions, the theoretical Li capacity of $\text{Mo}_2\text{TiC}_2\text{O}_2$ increases to $356 \text{ mA}\cdot\text{h g}^{-1}$. The latter value assumes that only one Li layer intercalates between the MXene layers. If more than one layer can intercalate,²⁶ the theoretical capacity could be significantly higher (e.g., doubled, if a double-layer of Li formed between the MXene sheets, etc.).²⁶

Similar to other MXenes, adsorption is not limited to Li^+ .²⁴ The adsorption energies of Li^+ , Na^+ , K^+ , Cs^+ , Mg^{2+} , Ca^{2+} and Al^{3+} ions on $\text{Mo}_2\text{TiC}_2(\text{OH})_2$, $\text{Mo}_3\text{C}_2(\text{OH})_2$ and $\text{Ti}_3\text{C}_2(\text{OH})_2$ surfaces were computationally investigated. For the OH terminated surfaces, only Cs^+ is stable (Supporting Information, Figure S9a). The rest presumably react with the OH terminations releasing H_2 and converting to O-terminated flakes.²⁶ When the same cations were absorbed onto $\text{Mo}_2\text{TiC}_2\text{O}_2$, $\text{Mo}_3\text{C}_2\text{O}_2$ and $\text{Ti}_3\text{C}_2\text{O}_2$ surfaces (i.e., assuming eq 1 was operative), the opposite was observed (Supporting Information, Figure 9b): Cs^+ was unstable, all the rest (with the exception of Al^{3+} on $\text{Ti}_3\text{C}_2\text{O}_2$) were stable.

Lastly, the enthalpy changes, at 0 K , assuming eq 2 is operative, for the various cations on the $\text{Mo}_2\text{TiC}_2\text{O}_2$, $\text{Mo}_3\text{C}_2\text{O}_2$ and $\text{Ti}_3\text{C}_2\text{O}_2$ surfaces (Supporting Information, Figure S9c) suggest that reaction 2 is operative for $\text{Mo}_2\text{TiC}_2\text{O}_2$ for all cations except Na^+ and K^+ . Said otherwise, $\text{Mo}_2\text{TiC}_2\text{O}_2$, could, in principle, be used as an electrode in Mg^{2+} , Ca^{2+} , and Al^{3+} -ion batteries.

Because $\text{Ti}_3\text{C}_2\text{T}_x$ has shown exceptional capacitance in aqueous electrolytes,²¹ we tested the capacitive behavior of $\text{Mo}_2\text{TiC}_2\text{T}_x$ 'paper' in $1 \text{ M H}_2\text{SO}_4$. While Mo is heavier than Ti and a lower gravimetric capacitance is expected, this difference in atomic weights should not significantly affect the volumetric capacitances. At potentials between -0.1 and 0.4 V , the CV curves obtained (Figure 6c) were more rectangular compared to those previously reported for $\text{Ti}_3\text{C}_2\text{T}_x$.³⁹ The working potential window also shifted by about 0.2 V to more positive potentials. The charge is expected to be stored by intercalated cations and possibly redox contributions from changes in the Mo oxidation state, similar to MoO_3 .⁴⁰ At a scan rate of 2 mV s^{-1} , the volumetric capacitance was calculated to be 413 F cm^{-3} and 78% of this capacitance was retained at 100 mV s^{-1} for a $3 \mu\text{m}$ thick film (Supporting Information, Figure S10a). Increasing the film thickness to $12 \mu\text{m}$ reduced the volumetric capacitance to 342 F cm^{-3} at a scan rate of 2 mV s^{-1} and 167 F cm^{-3} at a scan rate of 100 mV s^{-1} . Galvanostatic charge–discharge (GCD) tests at a 1 A g^{-1} current density showed perfect triangular shapes with negligible IR drops at the beginning of the charge and discharge cycles (inset in Figure 6d). GCD tests also showed no degradation in performance of the electrodes after $10\,000$ cycles (Figure 6d). Electrochemical impedance spectroscopy (EIS) tests show a near ideal behavior of the electrodes at low frequencies, with close to vertical slope of the Nyquist plots (Supporting Information, Figure S10b). There is no reason to believe that the high values reported in this work cannot be further improved by selecting other MXenes.

CONCLUSIONS

In summary, we predict that at 0 K , at least 26 ordered, double-M 2D carbides ($\text{M}'\text{M}''\text{Xene}$) should be stable. On the basis of the DFT calculations, we identified two general trends for the stabilities of these ordered MXenes. The first is that M-elements whose binary carbides do not crystallize in the rock salt structure, like Mo and Cr, avoid the center layers. The opposite is true for Nb and Ta; they prefer the middle layers. The relative stabilities of these compounds and their ordering could shift when entropy and surface terminations are taken into account. To verify DFT predictions, we synthesized $\text{Mo}_2\text{TiC}_2\text{T}_x$, $\text{Mo}_2\text{Ti}_2\text{C}_3\text{T}_x$ and $\text{Cr}_2\text{TiC}_x\text{T}_x$, and showed the electrochemical response of $\text{Mo}_2\text{TiC}_2\text{T}_x$ to be dominated by the surface Mo layers.

Lastly, we also expect nitrides and carbonitrides to show similar self-organizational behavior, further increasing the number of MXenes. It is reasonable to assume that the layering due to different sizes of M atoms will be even more pronounced in theoretically predicted MXene nanotubes,⁴¹ where placing smaller

atoms in the inner layer will decrease strain and stress, increasing nanotube stability. Thus, numerous new structures with different transition metals in outer and inner layers and various surface terminations are possible, greatly expanding the family MXenes in particular and 2D materials in general.

MATERIALS AND METHODS

Synthesis of MAX Phases. The Mo-based MAX phases were synthesized by ball milling Mo, Ti, Al and graphite powders (all from Alfa Aesar, Ward Hill, MA), with mesh sizes of ~250, ~325, ~325, and ~300, respectively, for 18 h using zirconia balls in plastic jars. The Mo/Ti/Al/C molar ratios were 2:1:1.2 and 2:2:1.3:2.7 for the $\text{Mo}_2\text{TiAlC}_2$ and $\text{Mo}_2\text{Ti}_2\text{AlC}_3$, respectively. Powder mixtures were heated in covered alumina crucibles at 5 °C/min to 1600 °C and held for 4 h under flowing argon. After cooling, the porous compacts were milled using a TiN-coated milling bit and sieved through a 400 mesh sieve, producing powders with a particle size <38 μm. Notably, this is the first report on the existence of the $\text{Mo}_2\text{Ti}_2\text{AlC}_3$ phase. $\text{Cr}_2\text{TiAlC}_2$ was synthesized by heating an elemental mixture of Cr, Ti, Al and C at 1500 °C for 1 h under Ar flow. Further details can be found in Supporting Information.

Synthesis of MXenes. Two grams of $\text{Mo}_2\text{TiAlC}_2$ or $\text{Mo}_2\text{Ti}_2\text{AlC}_3$ powders was added, over ≈60 s, to 20 ml of 48–51% aqueous HF solution and held at ambient temperature (55 °C for $\text{Mo}_2\text{Ti}_2\text{AlC}_3$) for 48 h (90 h for $\text{Mo}_2\text{Ti}_2\text{AlC}_3$) while stirring with a magnetic Teflon coated bar, rotating at 200 rpm. The mixtures were washed 5 times by adding distilled water, shaking for 1 min, centrifuging at 3500 rpm for 120 s for each cycle and finally decanted. After the last centrifugation, the pH of the supernatant was >6. The final product was mixed with distilled water and filtered on a membrane (3501 Coated PP, Celgard, Charlotte, NC). Cr_2TiC_2 synthesis is described in Supporting Information.

Preparation and Testing of LIB Electrodes. Electrodes were prepared by mixing the MXene powders, carbon black and 10 wt % polyvinylidene fluoride dissolved in 1-methyl-2-pyrrolidinone (all from Alfa Aesar, Ward Hill, MA) in a 80:10:10 ratio by weight. The mixture was coated onto a copper foil using a doctor blade and dried under vacuum at 140 °C for 24 h. Coin cells were assembled using Li foil and two layers of Celgard separators. The electrolyte was 1 M solution of LiPF₆ in a 1:1 mixture of ethylene carbonate and diethyl carbonate. Electrochemical studies were performed using a potentiostat (VMP3, Biologic, France).

Delamination of $\text{Mo}_2\text{TiC}_2\text{T}_x$ and Preparation of MXene 'Paper'. About 1 g of multilayered $\text{Mo}_2\text{TiC}_2\text{T}_x$ powder was mixed with 10 ml of DMSO and the mixture was stirred for 24 h at room temperature. The resulting colloidal suspension was centrifuged to separate the intercalated powder from the liquid DMSO. After decantation of the supernatant, 100 ml of deionized water was added to the residue and the mixture was sonicated for 1 h, before centrifuging it for 1 h at 3500 rpm. Lastly, the supernatant was decanted and filtered, using a Celgard membrane, and dried under vacuum.

Electrochemical Capacitor Fabrication and Testing. Electrodes based on multilayered $\text{Mo}_2\text{TiC}_2\text{T}_x$ were prepared by rolling a mixture of $\text{Mo}_2\text{TiC}_2\text{T}_x$ powders, acetylene carbon black (Alfa Aesar) and polytetrafluoroethylene (PTFE) binder (60 wt % solution in water, Aldrich, St. Louis MO). Rolled films, ~80 μm thick, were punched into 10 mm discs. The delaminated $\text{Mo}_2\text{TiC}_2\text{T}_x$ 'paper' was tested in 1 M H₂SO₄ electrolyte using 3-electrode Swagelok cells, where the MXene served as working electrode, an overcapacitive activated carbon film was used as a counter electrode, and Ag/AgCl in 1 M KCl was the reference electrode.³⁹

Microstructural Characterization. XRD was carried out on a Rigaku Smartlab (Tokyo, Japan) diffractometer using Cu Kα radiation (40 kV and 44 mA); step scan 0.02°, 3°–80° 2θ range, step time of 7 s, 10 × 10 mm² window slit. Ten wt % of silicon powder was

added to the MAX powders as an internal standard. A SEM (Zeiss Supra 50VP, Germany) equipped with EDX (Oxford Inca X-Sight, Oxfordshire, U.K.) was used. HR STEM and EDX analyses were carried out with a double corrected FEI Titan 3 operated at 300 kV, equipped with the Super-X EDX system. Selected area electron diffraction (SAED) characterization was performed using a FEI Tecnai G2 TF20 UT field emission microscope at 200 kV and a point resolution of 0.19 nm. The specimens were prepared by embedding the powder in a Ti grid, reducing the Ti-grid thickness down to 50 μm via mechanical polishing and finally Ar⁺ ion milling to reach electron transparency.

Density Functional Theory Simulations. First-principles calculations were carried out using DFT⁴² and the all-electron projected augmented wave (PAW)⁴³ method as implemented in the Vienna *ab initio* simulation package (VASP).⁴⁴ A plane-wave cutoff energy of 580 eV is sufficient to ensure convergence of the total energies to 1 meV per primitive cell. For the exchange-correlation energy, we used the Perdue-Burke-Ernzerhof (PBE) version of the generalized gradient approximation (GGA).⁴⁵ Considering the strong correlation effects in transition metals, electronic structure calculations and structural relaxations were performed using a spin-dependent GGA plus Hubbard U (GGA + U)⁴⁶ method. More details can be found in the Supporting Information.

Conflict of Interest: The authors declare no competing financial interest.

Acknowledgment. Synthesis of MAX phases and MXenes at Drexel University was funded by a grant from the U.S. Army Research Office under Grant Number W911NF-14-1-0568. We thank the Centralized Research Facility of Drexel University for access to XRD and SEM equipment. Electrochemical studies and DFT work were supported as part of the Fluid Interface Reactions, Structures and Transport (FIRST) Center, an Energy Frontier Research Center funded by the U.S. Department of Energy, Office of Science, Office of Basic Energy Sciences. This research used resources of the National Energy Research Scientific Computing Center, a DOE Office of Science User Facility supported by the Office of Science of the U.S. Department of Energy under Contract No. DE-AC02-05CH11231. The Linköping Electron Microscopy Laboratory was supported by the Knut and Alice Wallenberg Foundation. L.H., J.L., and M.W.B. acknowledge support from the Swedish Research Council. Crystal structures schematics were produced using VESTA.⁴⁷

Supporting Information Available: The Supporting Information is available free of charge on the ACS Publications website at DOI: 10.1021/acsnano.5b03591.

Computational details and full range of $\text{M}'_2\text{M}''\text{C}_2$ and $\text{M}'_2\text{M}''_2\text{C}_3$ configurations and complete energy profiles for all unterminated $\text{M}'\text{M}''\text{Xenes}$, EDX results of all the MAX and MXenes phases synthesized in this study, HR STEM with EDX of both Mo_2TiC_2 and $\text{Mo}_2\text{Ti}_2\text{C}_3$, TEM images of a Mo_2TiC_2 sheet and low-magnification TEM images of Mo_2TiC_2 and $\text{Mo}_2\text{Ti}_2\text{C}_3$, synthesis method of Cr_2TiC_2 , electrochemical performance of $\text{Mo}_2\text{TiC}_2\text{T}_x$ as LIB and supercapacitor electrodes, and ions adsorption energies on different MXenes (PDF)

REFERENCES AND NOTES

- Nicolosi, V.; Chhowalla, M.; Kanatzidis, M. G.; Strano, M. S.; Coleman, J. N. Liquid Exfoliation of Layered Materials. *Science* **2013**, 340, 1226419.

2. Geim, A.; Grigorieva, I. Van der Waals Heterostructures. *Nature* **2013**, *499*, 419–425.
3. Berger, C.; Song, Z.; Li, T.; Li, X.; Ogbazghi, A. Y.; Feng, R.; Dai, Z.; Marchenkov, A. N.; Conrad, E. H.; First, P. N.; et al. Ultrathin Epitaxial Graphite: 2D Electron Gas Properties and a Route toward Graphene-based Nanoelectronics. *J. Phys. Chem. B* **2004**, *108*, 19912–19916.
4. Allen, M. J.; Tung, V. C.; Kaner, R. B. Honeycomb Carbon: A Review of Graphene. *Chem. Rev.* **2010**, *110*, 132–145.
5. Geim, A. K. Graphene: Status and Prospects. *Science* **2009**, *324*, 1530–1534.
6. Lv, R.; Robinson, J. A.; Schaak, R. E.; Sun, D.; Sun, Y.; Mallouk, T. E.; Terrones, M. Transition Metal Dichalcogenides and Beyond: Synthesis, Properties, and Applications of Single- and Few-Layer Nanosheets. *Acc. Chem. Res.* **2015**, *48*, 56–64.
7. Gong, Y.; Liu, Z.; Lupini, A. R.; Shi, G.; Lin, J.; Najmaei, S.; Lin, Z.; Elias, A. L.; Berkdemir, A.; You, G.; et al. Band Gap Engineering and Layer-by-Layer Mapping of Selenium-Doped Molybdenum Disulfide. *Nano Lett.* **2014**, *14*, 442–449.
8. Butler, S. Z.; Hollen, S. M.; Cao, L.; Cui, Y.; Gupta, J. A.; Gutiérrez, H. R.; Heinz, T. F.; Hong, S. S.; Huang, J.; Ismach, A. F.; et al. Progress, Challenges, and Opportunities in Two-Dimensional Materials Beyond Graphene. *ACS Nano* **2013**, *7*, 2898–2926.
9. Taha-Tijerina, J.; Narayanan, T. N.; Gao, G.; Rohde, M.; Tsentalovich, D. A.; Pasquali, M.; Ajayan, P. M. Electrically Insulating Thermal Nano-Oils Using 2D Fillers. *ACS Nano* **2012**, *6*, 1214–1220.
10. Wang, Q. H.; Kalantar-Zadeh, K.; Kis, A.; Coleman, J. N.; Strano, M. S. Electronics and Optoelectronics of Two-Dimensional Transition Metal Dichalcogenides. *Nat. Nanotechnol.* **2012**, *7*, 699–712.
11. Osada, M.; Sasaki, T. Exfoliated Oxide Nanosheets: New Solution to Nanoelectronics. *J. Mater. Chem.* **2009**, *19*, 2503–2511.
12. Sugimoto, W.; Iwata, H.; Yasunaga, Y.; Murakami, Y.; Takasu, Y. Preparation of Ruthenic Acid Nanosheets and Utilization of Its Interlayer Surface for Electrochemical Energy Storage. *Angew. Chem., Int. Ed.* **2003**, *42*, 4092–4096.
13. Rui, X.; Lu, Z.; Yu, H.; Yang, D.; Hng, H. H.; Lim, T. M.; Yan, Q. Ultrathin V_2O_5 Nanosheet Cathodes: Realizing Ultrafast Reversible Lithium Storage. *Nanoscale* **2013**, *5*, 556–560.
14. Naguib, M.; Come, J.; Dyatkin, B.; Presser, V.; Taberna, P.-L.; Simon, P.; Barsoum, M. W.; Gogotsi, Y. MXene: A Promising Transition Metal Carbide Anode for Lithium-Ion Batteries. *Electrochem. Commun.* **2012**, *16*, 61–64.
15. Naguib, M.; Kurtoglu, M.; Presser, V.; Lu, J.; Niu, J.; Heon, M.; Hultman, L.; Gogotsi, Y.; Barsoum, M. W. Two-Dimensional Nanocrystals Produced by Exfoliation of Ti_3AlC_2 . *Adv. Mater.* **2011**, *23*, 4248–4253.
16. Naguib, M.; Mochalin, V. N.; Barsoum, M. W.; Gogotsi, Y. MXenes: A New Family of Two-Dimensional Materials. *Adv. Mater.* **2014**, *26*, 982–982.
17. Naguib, M.; Halim, J.; Lu, J.; Cook, K. M.; Hultman, L.; Gogotsi, Y.; Barsoum, M. W. New Two-Dimensional Niobium and Vanadium Carbides as Promising Materials for Li-ion Batteries. *J. Am. Chem. Soc.* **2013**, *135*, 15966–15969.
18. Kurtoglu, M.; Naguib, M.; Gogotsi, Y.; Barsoum, M. W. First Principles Study of Two-Dimensional Early Transition Metal Carbides. *MRS Commun.* **2012**, *2*, 133–137.
19. Hu, Q.; Wang, H.; Wu, Q.; Ye, X.; Zhou, A.; Sun, D.; Wang, L.; Liu, B.; He, J. Two-Dimensional Sc_2C : A Reversible and High-Capacity Hydrogen Storage Material Predicted by First-Principles Calculations. *Int. J. Hydrogen Energy* **2014**, *39*, 10606–10612.
20. Khazaei, M.; Arai, M.; Sasaki, T.; Chung, C.-Y.; Venkataraman, N. S.; Estili, M.; Sakka, Y.; Kawazoe, Y. Novel Electronic and Magnetic Properties of Two-Dimensional Transition Metal Carbides and Nitrides. *Adv. Funct. Mater.* **2013**, *23*, 2185–2192.
21. Ghidiu, M.; Lukatskaya, M. R.; Zhao, M.-Q.; Gogotsi, Y.; Barsoum, M. W. Conductive Two-Dimensional Titanium Carbide 'Clay' with High Volumetric Capacitance. *Nature* **2014**, *516*, 78–81.
22. Liang, X.; Garsuch, A.; Nazar, L. F. Sulfur Cathodes Based on Conductive MXene Nanosheets for High-Performance Lithium–Sulfur Batteries. *Angew. Chem., Int. Ed.* **2015**, *54*, 3907–3911.
23. Mashtalir, O.; Naguib, M.; Mochalin, V. N.; Dall'Agnese, Y.; Heon, M.; Barsoum, M. W.; Gogotsi, Y. Intercalation and Delamination of Layered Carbides and Carbonitrides. *Nat. Commun.* **2013**, *4*, 1716.
24. Xie, Y.; Dall'Agnese, Y.; Naguib, M.; Gogotsi, Y.; Barsoum, M. W.; Zhuang, H. L.; Kent, P. R. C. Prediction and Characterization of MXene Nanosheet Anodes for Non-Lithium-Ion Batteries. *ACS Nano* **2014**, *8*, 9606–9615.
25. Tang, Q.; Zhou, Z.; Shen, P. Are MXenes Promising Anode Materials for Li Ion Batteries? Computational Studies on Electronic Properties and Li Storage Capability of Ti_3C_2 and $Ti_3C_2X_2$ ($X = F, OH$) Monolayer. *J. Am. Chem. Soc.* **2012**, *134*, 16909–16916.
26. Xie, Y.; Naguib, M.; Mochalin, V. N.; Barsoum, M. W.; Gogotsi, Y.; Yu, X.; Nam, K.-W.; Yang, X.-Q.; Kolesnikov, A. I.; Kent, P. R. C. Role of Surface Structure on Li-Ion Energy Storage Capacity of Two-Dimensional Transition-Metal Carbides. *J. Am. Chem. Soc.* **2014**, *136*, 6385–6394.
27. Er, D.; Li, J.; Naguib, M.; Gogotsi, Y.; Shenoy, V. B. Ti_3C_2 MXene as a High Capacity Electrode Material for Metal (Li, Na, K, Ca) Ion Batteries. *ACS Appl. Mater. Interfaces* **2014**, *6*, 11173–11179.
28. Liu, Z.; Zheng, L.; Sun, L.; Qian, Y.; Wang, J.; Li, M. $(Cr_{2/3}Ti_{1/3})_3AlC_2$ and $(Cr_{5/8}Ti_{3/8})_4AlC_3$: New MAX-phase Compounds in Ti–Cr–Al–C System. *J. Am. Ceram. Soc.* **2014**, *97*, 67–69.
29. Anasori, B.; Halim, J.; Lu, J.; Voigt, C. A.; Hultman, L.; Barsoum, M. W. Mo_2TiAlC_2 : A New Ordered Layered Ternary Carbide. *Scr. Mater.* **2015**, *101*, 5–7.
30. Anasori, B.; Dahlqvist, M.; Halim, J.; Moon, E. J.; Lu, J.; Hosler, B. C.; Caspi, E. N.; May, S.; Hultman, L.; Eklund, P.; Rosén, J.; Barsoum, M. W. Experimental and Theoretical Characterization of Ordered MAX Phases Mo_2TiAlC_2 and $Mo_2Ti_2AlC_3$. *J. Appl. Phys.* **2015**, In Press.
31. Hugosson, H. W.; Eriksson, O.; Nordström, L.; Jansson, U.; Fast, L.; Delin, A.; Wills, J. M.; Johansson, B. Theory of Phase Stabilities and Bonding Mechanisms in Stoichiometric and Substoichiometric Molybdenum Carbide. *J. Appl. Phys.* **1999**, *86*, 3758–3767.
32. Enyashin, A. N.; Ivanovskii, A. L. Two-Dimensional Titanium Carbonitrides and Their Hydroxylated Derivatives: Structural, Electronic Properties and Stability of MXenes $Ti_{3}C_{2-x}N_x(OH)_2$ from DFTB Calculations. *J. Solid State Chem.* **2013**, *207*, 42–48.
33. Ghidiu, M.; Naguib, M.; Shi, C.; Mashtalir, O.; Pan, L. M.; Zhang, B.; Yang, J.; Gogotsi, Y.; Billinge, S. J. L.; Barsoum, M. W. Synthesis and Characterization of Two-Dimensional Nb_4C_3 (MXene). *Chem. Commun.* **2014**, *50*, 9517–9520.
34. Wang, X.; Kajiyama, S.; Iinuma, H.; Hosono, E.; Oro, S.; Moriguchi, I.; Okubo, M.; Yamada, A. Pseudocapacitance of MXene Nanosheets for High-Power Sodium-Ion Hybrid Capacitors. *Nat. Commun.* **2015**, *6*, 6544.
35. Peng, Q.; Guo, J.; Zhang, Q.; Xiang, J.; Liu, B.; Zhou, A.; Liu, R.; Tian, Y. Unique Lead Adsorption Behavior of Activated Hydroxyl Group in Two-Dimensional Titanium Carbide. *J. Am. Chem. Soc.* **2014**, *136*, 4113–4116.
36. Meduri, P.; Clark, E.; Kim, J. H.; Dayalan, E.; Sumanasekera, G. U.; Sunkara, M. K. MoO_{2-x} Nanowire Arrays As Stable and High-Capacity Anodes for Lithium Ion Batteries. *Nano Lett.* **2012**, *12*, 1784–1788.
37. Stephenson, T.; Li, Z.; Olsen, B.; Mitlin, D. Lithium Ion Battery Applications of Molybdenum Disulfide (MoS_2) Nanocomposites. *Energy Environ. Sci.* **2014**, *7*, 209–231.
38. Liu, Y.; Zhang, H.; Ouyang, P.; Chen, W.; Wang, Y.; Li, Z. High Electrochemical Performance and Phase Evolution of Magnetron Sputtered MoO_2 Thin Films with Hierarchical Structure for Li-Ion Battery Electrodes. *J. Mater. Chem. A* **2014**, *2*, 4714–4721.
39. Lukatskaya, M. R.; Mashtalir, O.; Ren, C. E.; Dall'Agnese, Y.; Rozier, P.; Taberna, P. L.; Naguib, M.; Simon, P.; Barsoum, M. W.; Gogotsi, Y. Cation Intercalation and High Volumetric

- Capacitance of Two-Dimensional Titanium Carbide. *Science* **2013**, *341*, 1502–1505.
40. Brezesinski, T.; Wang, J.; Tolbert, S. H.; Dunn, B. Ordered Mesoporous [alpha]-MoO₃ with Iso-Oriented Nanocrystalline Walls for Thin-Film Pseudocapacitors. *Nat. Mater.* **2010**, *9*, 146–151.
41. Enyashin, A.; Ivanovskii, A. Atomic Structure, Comparative Stability and Electronic Properties of Hydroxylated Ti₂C and Ti₃C₂ Nanotubes. *Comput. Theor. Chem.* **2012**, *989*, 27–32.
42. Kohn, W.; Sham, L. J. Self-Consistent Equations Including Exchange and Correlation Effects. *Phys. Rev.* **1965**, *140*, A1133.
43. Blöchl, P. E. Projector Augmented-Wave Method. *Phys. Rev. B: Condens. Matter Mater. Phys.* **1994**, *50*, 17953.
44. Kresse, G.; Furthmüller, J. Efficient Iterative Schemes for Ab Initio Total-Energy Calculations Using a Plane-Wave Basis Set. *Phys. Rev. B: Condens. Matter Mater. Phys.* **1996**, *54*, 11169.
45. Perdew, J. P.; Burke, K.; Ernzerhof, M. Generalized Gradient Approximation Made Simple. *Phys. Rev. Lett.* **1996**, *77*, 3865.
46. Dudarev, S.; Botton, G.; Savrasov, S.; Humphreys, C.; Sutton, A. Electron-Energy-Loss Spectra and the Structural Stability of Nickel Oxide: An LSDA+ U Study. *Phys. Rev. B: Condens. Matter Mater. Phys.* **1998**, *57*, 1505.
47. Momma, K.; Izumi, F. VESTA 3 for Three-Dimensional Visualization of Crystal, Volumetric and Morphology Data. *J. Appl. Crystallogr.* **2011**, *44*, 1272–1276.